Organic Electronics 14 (2013) 2476–2483

Contents lists available at SciVerse ScienceDirect

Organic Electronics

journal homepage: www.elsevier.com/locate/orgel

The dual localized surface plasmonic effects of gold nanodots and gold nanoparticles enhance the performance of bulk heterojunction polymer solar cells

Chih-Ming Liu, Chia-Min Chen, Yu-Wei Su, Shu-Min Wang, Kung-Hwa Wei *

Department of Materials Science and Engineering, National Chiao Tung University, Hsinchu 30049, Taiwan

ARTICLE INFO

Article history:
Received 6 March 2013
Received in revised form 17 June 2013
Accepted 18 June 2013
Available online 1 July 2013

Keywords:
Polymer solar cells
Localized surface plasmon resonance
Gold nanoparticles
Gold nanodots

ABSTRACT

In this study, we investigated the effects of plasmonic resonances induced by gold nanodots (Au NDs), thermally deposited on the active layer, and octahedral gold nanoparticles (Au NPs), incorporated within the hole transport layer, on the performance of bulk heterojunction polymer solar cells (PSCs) based on poly(3-hexyl thiophene) (P3HT) and [6,6]-phenyl-C_{61}butyric acid methyl ester ($PC_{61}BM$). Thermal deposition of 5.3-nm Au NDs between the active layer and the cathode in a P3HT:$PC_{61}BM$ device resulted in the power conversion efficiency (PCE) of 4.6%—that is 15% greater than that (4.0%) for the P3HT:$PC_{61}BM$ device without Au NDs. The Au NDs provided near-field enhancement through excitation of the localized surface plasmon resonance (LSPR), thereby enhancing the degree of light absorption.

In addition to the thermally deposited Au-NDs, embedding Au NPs within the poly(3,4-ethylenedioxythiophene):poly(styrenesulfonate) (PEDOT:PSS) to form a dual metallic nanostructure can further enhance PCE to 4.8%—that is about 20% greater than that of the conventional P3HT:$PC_{61}BM$ cell. Thus, Au NPs and Au NDs appear to have great potential for the application in high-efficiency LSPR-enhanced PSCs.

1. Introduction

The development of conjugated polymers for use in organic optoelectronic devices has been an area of extensive investigation because of their potential applications as cheap, large-area, flexible devices [1–3], bulk heterojunction (BHJ) polymer solar cells (PSCs) [4], incorporating conjugated polymers and fullerene derivatives as electron donors and acceptors, respectively, have been the most widely investigated PSC systems because of their efficient exciton dissociation, tunable energy bands and solubility of the materials involved and simple processing. The power conversion efficiencies (PCEs) of PSCs featuring P3HT and $PC_{61}BM$ [5] as the photoactive layer have reached approximately 4% [6–11]. The signature optical property of noble metal nanoparticles (NPs) is their localized surface plasmon resonance (LSPR) [12–18], a phenomenon in which metal NPs excited by electromagnetic radiation exhibit collective oscillations of their conduction electrons. LSPR-enhanced absorption arises from the resonant electromagnetic behavior of the metal NPs—that is, it arises from the confinement of the conduction electrons within the small particle volume. For particles having a diameter (d) much smaller than the wavelength of the radiation (λ), the electrons within the particle all move in phase upon plane-wave excitation, leading to the buildup of polarization charges on the particle surface. Thus, the resonantly enhanced field arises within the whole volume of a small particle, and produces a dipolar field outside the particle. This phenomenon leads to enhanced light absorption and scattering cross sections for electromagnetic waves, as well as a strongly enhanced near field in the vicinity of the particle surface.

* Corresponding author. Tel.: +886 3 5712121x31871; fax: +886 3 5724727.
E-mail address: khwei@mail.nctu.edu.tw (K.-H. Wei).

1566-1199/$ - see front matter © 2013 Published by Elsevier B.V.
http://dx.doi.org/10.1016/j.orgel.2013.06.012

The wavelength corresponding to the maximum extinction, λ_{max}, of the LSPR is highly dependent on the size, shape, and dielectric properties of the metal NPs [19]. The primary consequences of LSPR are the appearance of intense surface plasmon absorption bands and an enhancement of the local electromagnetic fields. The frequency and intensity of the surface plasmon absorption bands are characteristic of the types of materials (typically Au, Ag, Cu or Pt), and highly sensitive to the size, size distribution, and shape of the nanostructures, as well as the surrounding environments [17,20–23]. Recently, the improvements in PCEs have been demonstrated in BHJ PSCs and small-molecule solar cells, ascribed mainly to the light concentrating effect caused by plasmonic scattering or near-field enhancement [24–28]. Surface plasmon resonance of metal NPs can also modify the intrinsic properties of nearby fluorophores [29], and cause the quench emissions of fluorophores in the vicinity of metal NPs [30].

To obtain high PCEs in BHJ PSCs, it would be desirable to increase the absorption of the active layer without increasing its thickness, because a thicker layer usually leads to a higher probability of carrier recombination. Metal nanostructures exhibit LSPRs that couple strongly to the incident light have been used previously to enhance the performance of BHJ PSCs—for example, by introducing metallic NPs in the carrier transport layer [24–27,31–34], into the active layer of bulk junctions [28,35–39], or on top of the active layer [40,41], in most cases when used in combination with P3HT.

Several studies reported using embedded metal NPs in optical dielectric materials [42–44]. A common method for forming such monolayer films involves the organic synthesized colloidal particles with ligands [45–47]. Nevertheless, such films often exhibit inconsistent properties due to the aggregation of particles. Light scattering from a small metal NP embedded in a homogeneous medium is nearly symmetric in the forward and reverse directions.

In addition, this colloidal solution process has difficulty on controlling the density and stability of the films. To solve these problems, we deposited gold nanodots (Au NDs) directly onto the active layer using thermal evaporation. Compared to the colloidal solution process, thermal evaporation process has high throughput to produce high density Au NDs [41].

The shapes of the Au NDs depend mainly on the surface energy of the material upon which they are to be deposited; Au NDs are formed in their lowest energy state when the Au surface and the surface tension are balanced in the structure. Au NDs are in the shape of hemi-spherical or spherical. It has been noted that Au NDs having the minimum surface energy will feature oblate or prolate structures, with greater deviation from the spherical [48–50]. In this study, two types of metallic nanostructures—Au NPs embedded in the PEDOT:PSS layer and Au NDs thermally deposited on the active layer—were added in the conventional BHJ (P3HT:$PC_{61}BM$) solar cells. We expected the LSPR effect from dual Au structure (glass/ITO/PEDOT:PSS:AuNPs/P3HT:$PC_{61}PM$/Au NDs/Ca/Al) would improve the PCE. According to optical and electrical analyses, the LSPR enhanced the light absorption efficiency through two separate pathways: the optical path length was increased through scattering effects and a strong near field was induced to enhance the absorption of the active layer. Our experimental results suggest an approach toward optimizing plasmonic PSCs structures through the use of simple processing methods.

2. Experimental

2.1. PSCs device fabrication

The PSCs devices were fabricated on an ITO-coated glass substrate. After a routine cleaning process, the substrate was dried and treated with UV ozone. The Au NPs solution was prepared using the previously described procedures [51]. To prepare the anodic buffer layer, 2 mg Au NPs was blended into 1 mL 1.5 wt% PEDOT:PSS (Baytron 4071) solution. The blended solution was spin-coated onto an ITO-coated glass substrate, and then thermally annealed at 150 °C for 15 min, giving a 12 wt% Au NPs in the composite film of PEDOT:PSS and Au NPs. Extra PEDOT:PSS was spin-coated as a thinner capping layer to decrease the surface roughness of the anodic buffer layer. The thickness of the capping PEDOT:PSS layer is about 10 nm, which is determined using α-step measurement. Equal weight of P3HT (Rieke Metals) and $PC_{61}BM$ (Solenne BV) were mixed, and dissolved in the dichlorobenzene (DCB) (Sigma–Aldrich) in a concentration of 40 mg/mL. The P3HT:$PC_{61}BM$ solution was agitated at 80 °C until all solutes dissolved completely. The mixture solution was spin-coated onto the anodic buffer layer to provide an active layer (ca. 150 nm). Au NDs were deposited onto the active layer through thermal evaporation at a pressure of 5×10^{-7} torr and a deposition speed of 0.1 Å/s. The resulted Au NDs average sizes of 2.7, 3.1, 4.5, and 5.3 nm were obtained by various deposition times. Top contacts of Ca (15 nm) and Al (100 nm) were sequentially thermally evaporated onto the Au NDs.

2.2. Characterisation

The current density (J)–voltage (V) characteristics of the finished devices were evaluated by using a Keithley Model 2400 source meter under illumination intensity of 100 mW/cm^2 from a solar simulator (Newport 66902) with AM 1.5G filter. EQEs were measured by using a spectral response measurement set-up (Optosolar SR150). The active layer of a finished device was detached in DI water and transferred to a Cu foil grid for top-view TEM imaging operated at 120 keV (FEI Tecnai G2). Focused ion beam was used for cross-sectional TEM imaging. Steady state PL spectra were recorded under ambient condition in air using an F-7000 fluorescence spectrophotometer. Samples for the PL study were prepared in the same manner as the active layers used in the devices without $PC_{61}BM$. The only difference is the film was made on Silicon substrate instead of ITO-coated glass. Time-resolved PL spectra of the P3HT:$PC_{61}BM$ films were measured using a home-built single photon counting system (Horiba Jobin Yvon). A GaN diode laser (λ = 470 nm) with the pulse duration of 50 ps was used as the excitation source. The signals

collected at 650 nm were dispersed with a grating spectrometer, detected by a high-speed photomultiplier tube, and then correlated using a single photon counting card.

3. Results and discussion

3.1. The performance of bulk heterojunction photovoltaic devices with Au NDs on the top of the active layer

Fig. 1 displays a schematic diagram of a dual metallic plasmonic nanostructured PSC device with the structure of glass/ITO/PEDOT:PSS:50-nm Au NPs/P3HT:$PC_{61}BM$ (150 nm)/Au NDs/Ca (15 nm)/Al (100 nm). The number in bracket represents the film thickness of each layer. The size of the thermally deposited Au NDs on P3HT:$PC_{61}BM$ active layer could be tuned by adjusting the depositing parameters. We first studied on how the size of Au NDs affects the device performance. Then, Au NPs was incorporated into the device which has the optimized Au NDs for the highest PCE.

Fig. 2a displays the current density–voltage (J–V) characteristics of P3HT:$PC_{61}BM$ devices incorporating various sizes of Au NDs. The detailed photovoltaic parameters are listed in Table 1. Compared to the reference device (without Au-NDs), the PCE was increased appreciably upon increasing the average size of Au NDs greater than 4.5 nm. The PCE was increased to 4.3% in the case of the 4.5-nm Au NDs from 4.0% of the reference device. Keep increasing the Au NDs to 5.3 nm, the PCE was increased further to 4.6% —an increase of 15% than the reference cell. The short-circuit current density (J_{sc}) was enhanced from 9.2 mA/cm^2 (reference) to 10.6 mA/cm^2 (5.3-nm Au NDs). The open-circuit voltages (V_{oc}) and fill factors (FFs) of these devices remained similar. This 15% increase in J_{sc} was presumably caused by the greater degree of light absorption in the P3HT:$PC_{61}BM$/Au NDs active layer than that in the pure P3HT:$PC_{61}BM$ active layer, due to the plasmonic effect of the deposited Au NDs.

Fig. 2b displays the external quantum efficiencies (EQEs) of these devices. The absorption range from 360 to 620 nm shows the larger Au NDs can result higher EQE. The integrated values of J_{sc} determined from our EQE spectra for the devices incorporating the 2.7-, 3.1-, 4.5-, and 5.3-nm Au NDs were 9.6, 9.6, 10.0 and 10.6 mA/cm^2, respectively. The differences between the integrated values of J_{sc} from the EQE curves and the measured values of J_{sc} were within 3%, indicating the high accurate measurements.

Fig. 2c presents the corresponding UV–Vis absorption curves for the Au NDs having average dimensions ranging

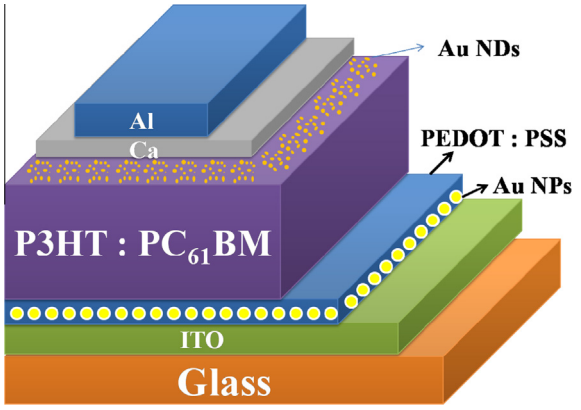

Fig. 1. Schematic representation of the dual plasmonic structured device. From bottom to top: ITO/PEDOT:PSS:50-nm Au NPs/P3HT:$PC_{61}BM$ (150 nm)/5.3-nm Au NDs/Ca (15 nm)/Al (100 nm).

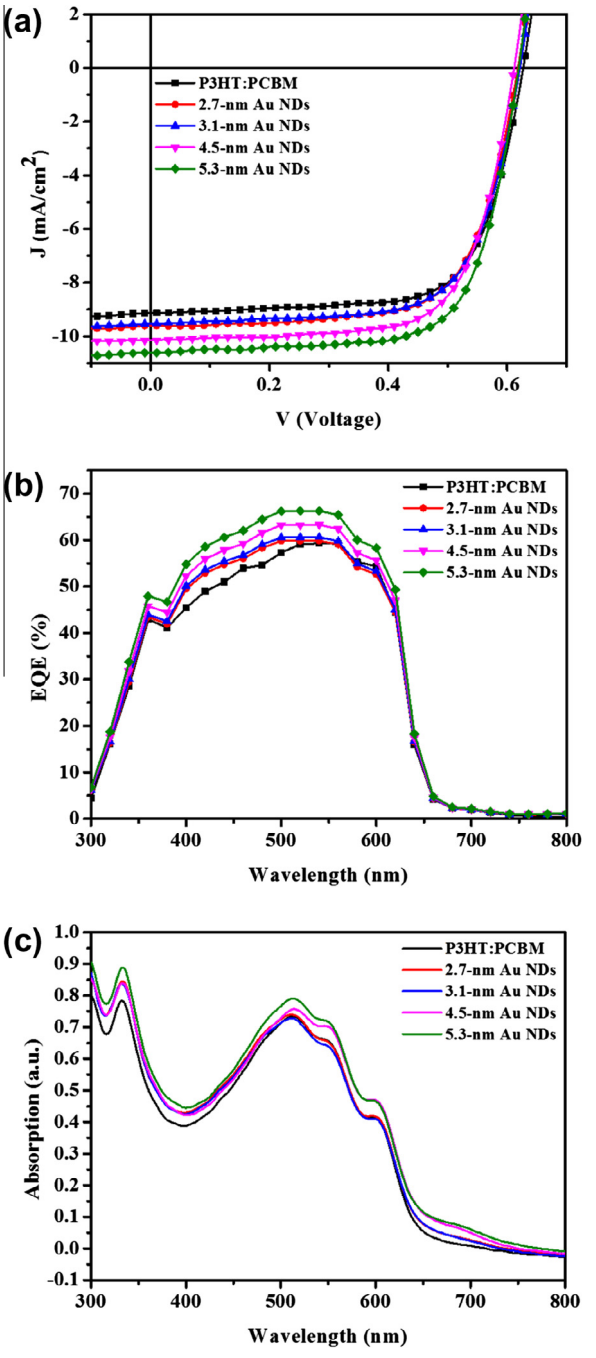

Fig. 2. (a) J–V and (b) EQE curves of devices incorporating P3HT:$PC_{61}BM$ (ca. 150 nm) and thermally evaporated Au NDs. (c) Absorption spectra of P3HT:$PC_{61}BM$ films presenting Au NDs deposited through thermal evaporation.

Table 1
Performance of PSCs featuring PEDOT:PSS layers prepared with or without thermally evaporated Au NDs or incorporated 50-nm Au NPs.

Device	V_{oc} (V)	J_{sc} (mA/cm^2)	FF (%)	PCE (%)
Reference	0.63 ± 0.02	9.21 ± 0.08	69.3 ± 0.2	4.02 ± 0.17
2.7-nm Au NDs	0.62 ± 0.01	9.60 ± 0.13	68.2 ± 0.3	4.06 ± 0.13
3.1-nm Au NDs	0.62 ± 0.01	9.62 ± 0.18	68.2 ± 0.2	4.07 ± 0.15
4.5-nm Au NDs	0.61 ± 0.01	10.03 ± 0.11	70.2 ± 0.1	4.30 ± 0.12
5.3-nm Au NDs	0.62 ± 0.01	10.58 ± 0.15	70.9 ± 0.2	4.65 ± 0.15
6.2-nm Au NDs	0.62 ± 0.02	9.76 ± 0.21	69.1 ± 0.2	4.18 ± 0.23
Au NPs (50 nm) + Au NDs (5.3 nm)	0.64 ± 0.01	11.20 ± 0.09	67.0 ± 0.2	4.80 ± 0.12

from 2.7 to 5.3 nm on the P3HT:PC_{61}BM films. The absorption peak at 334 nm and 512 nm was contributed to the PC_{61}BM and P3HT, respectively. The deposited 2.7- and 3.1-nm Au NDs slightly enhanced the absorptions of the P3HT:PC_{61}BM films from 300 to 512 nm, while the deposited 4.5- and 5.3-nm Au NDs increased the absorptions of the P3HT:PC_{61}BM films from 300 to 800 nm, with the absorption of the P3HT:PC_{61}BM film incorporating the 5.3-nm Au NDs being greater than that of the film incorporating the 4.5-nm Au NDs. This trend is consistent with that for the light absorption of the Au NDs; the UV–Vis spectra of the Au NDs deposited through thermal evaporation onto the PEDOT:PSS/ITO substrate (Fig. 3) reveal that the absorption peaks for the plasmonic resonance become more pronounced and were slightly red-shifted upon increasing the average size of the Au NDs. Specifically, the LSPR peak shifted from being barely distinguishable at 552 nm for the 4.5-nm Au NDs to 576 nm for the 5.3-nm Au NDs. Because of the low absorption intensities of the Au NDs, we believe that the enhanced light absorption of the P3HT:PC_{61}BM films resulted from the optical near-field, which was generated by surface plasmons and was associated with the localized plasmons of the nanosized particles.

3.2. TEM results

Fig. 4a presents a top-view TEM image of the pure P3HT:PC_{61}BM film, revealing its rather homogeneous structure. Fig. 4b–e display the corresponding images of the 2.7-, 3.1-, 4.5-, and 5.3-nm Au NDs, respectively, that had been deposited directly onto the active layer; here, we varied the average size of the Au NDs by tuning the deposition conditions. The inset figures are the size distribution charts of Au NDs. Fig. 4e reveals that the mean distance between two neighboring 5.3-nm Au NDs was approximately 9.8 nm—much smaller that the wavelength of the incident light, suggesting that their interactions in the vicinity of the particle surface occurred through a near-field–dominated process [22]. Fig. 4f presents a cross-sectional TEM image of the 5.3-nm Au NDs on the P3HT:PC_{61}BM active layer surface and embedded in the Ca electrode. The reason that Au NDs can form a dense layer instead of protruding into P3HT:PC_{61}BM active layer surface was controlling the deposition condition in high vacuum (5×10^{-7} torr) and low deposition rate (0.1 Å/s). This smooth active layer surface was an important aspect of the efficient operation of the corresponding device.

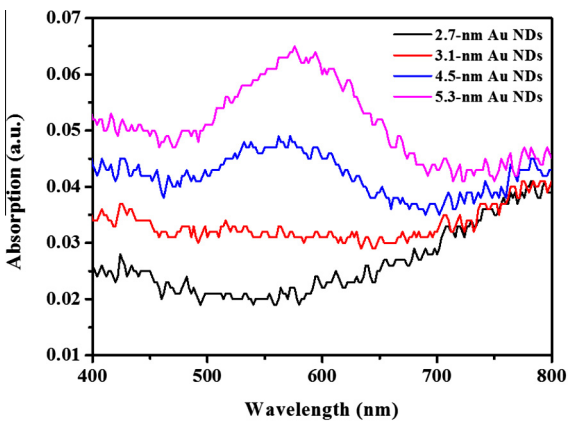

Fig. 3. UV–Vis spectra of PEDOT:PSS/ITO substrates presenting Au NDs deposited through thermal evaporation.

3.3. Polymer solar cell performance of dual metallic nanostructure (Au NDs plus Au NPs)

Fig. 5a displays the photovoltaic performances of the devices incorporating both the 50-nm octahedral Au NPs in the PEDOT:PSS layer and the 5.3-nm Au NDs on the active layer. Table 1 lists the detailed photovoltaic parameters. We have compared the phovoltaic performances of the devices incorporating either 30- or 50-nm octahedral Au NPs for being blended in the PEDOT:PSS layer for LSPR effect (see Fig. S3 and Table S1), and decided to adopt 50-nm octahedral Au NPs for this study. Fig. S2 shows the UV–Vis spectra of pristine P3HT:PC_{61}BM with 30- or 50-nm octahedral Au nanoparticles incorporating in the PEDOT:PSS layer, and the 50-nm Au NPs appears to have better absorption than that of 30-nm Au NPs case.

The PCE of the dual metallic nanostructured P3HT:PC_{61}BM device incorporating both the 5.3-nm Au NDs and the 50-nm Au NPs increased to 4.8% from a value of 4.0% for the pristine P3HT:PC_{61}BM device. We suspect that the dual plasmon effects enhanced the absorption of incident light in the active layer and increased the effective optical path length; that is, when light entered the PEDOT:PSS:Au NPs layer, the light scattering and LSPR effects of the Au NPs presumably increased the effective optical path length and enhanced the optical absorption of the P3HT:PC_{61}BM film. The Au NDs also had the effect of trapping the incident light in the active layer [25–28]. Fig. 5b and c respectively display the EQE curve and UV–Vis spectra of the device with dual metallic nanostructure. The intensities

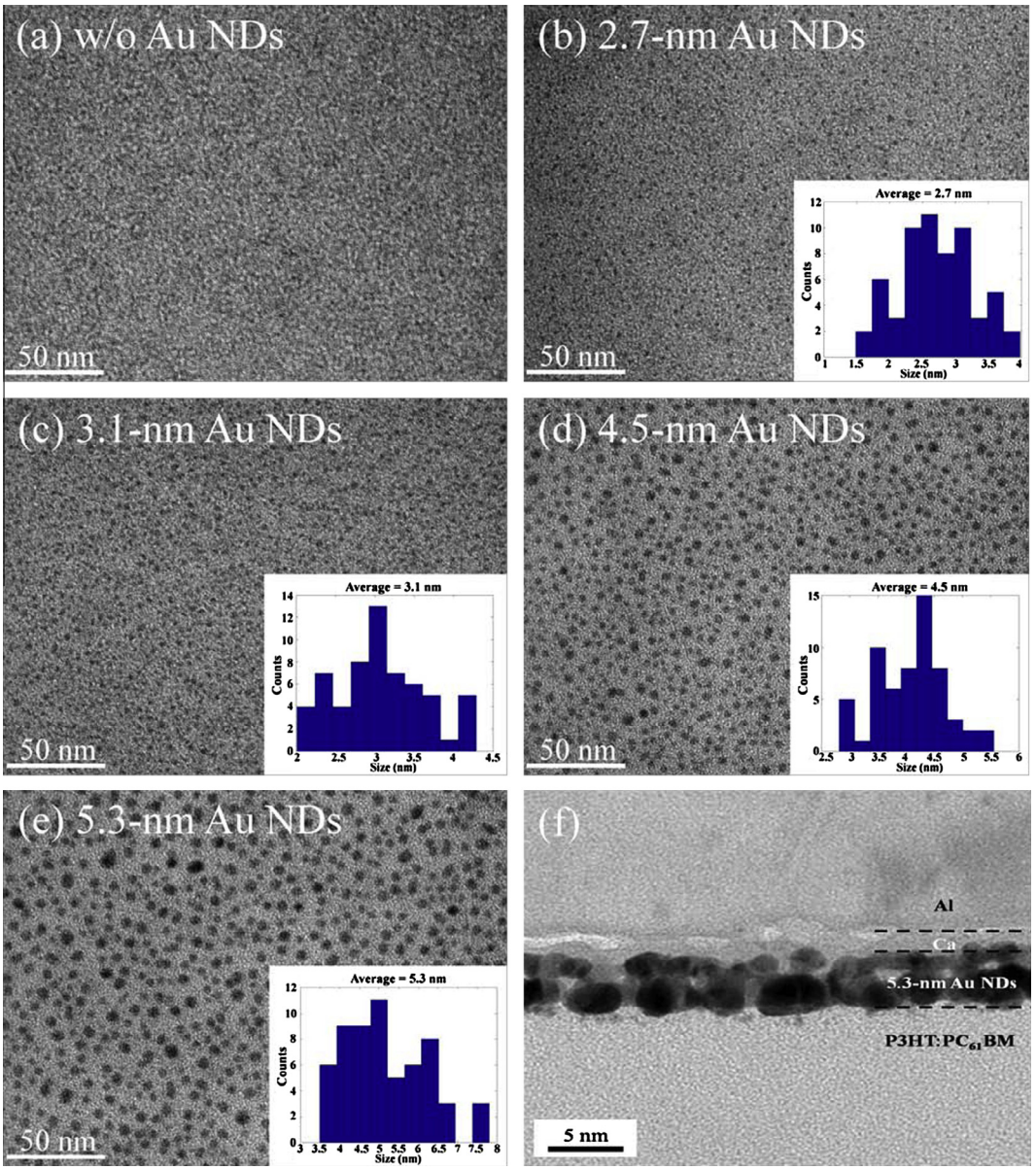

Fig. 4. Top-view TEM images of P3HT:$PC_{61}BM$ films without (a) and with 2.7-, 3.1-, 4.5-, and 5.3-nm (b–e) thermal evaporated Au NDs. (f) Cross-sectional TEM image of thermally evaporated 5.3-nm Au NDs on a P3HT:$PC_{61}BM$ film. (Inset: size distribution chart of Au NDs).

of the signals in both figures were enhanced as a result of the presence of the dual metallic nanostructure; this increased absorption contributed to the increased photocurrent, relative to that of the pristine P3HT:$PC_{61}BM$, and thereby contributed to the improvement in the value of J_{sc}.

By plotting together the absorption enhancement spectra of the Au NDs–only and combined Au NDs/Au NPs devices, we confirmed that the absorption enhancement provided by the combined 50-nm metallic NPs and 5.3-nm Au NDs contributed to the improvement in the values of J_{sc} and PCE of the PSCs featuring the dual plasmonic nanostructure. In terms of the optical effects arising from the dual plasmonic structures, we observed similar trends in the increasing EQEs and absorptions of device incorporating the two types of metal nanostructure (Fig. 5b and c, respectively). The integrated value of J_{sc} determined from the EQE spectrum for the device featuring the 5.3-nm Au NDs and the 50-nm Au NPs in the PEDOT:PSS layer was 10.9 mA/cm^2. The difference between integrated and measured values of J_{sc} was within 3%, again indicating the high accuracy of our PSC measurements.

The photo-current of the device increased significantly when the active layer incorporated thermally deposited Au NDs. This wavelength regime 360-620 nm coincides with the extinction range of the Au NDs, indicating that LSPR effects were responsible for the improved photo current. To study the LSPR effect on the active layer, we chose the octahedral Au NPs to concentrate the light through their

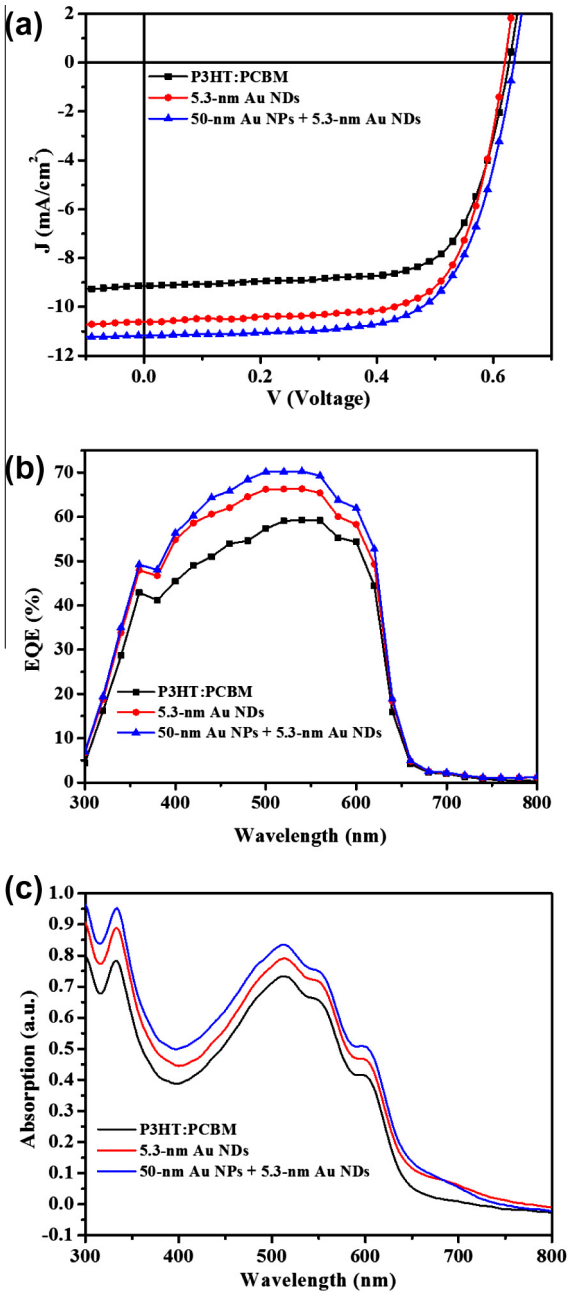

Fig. 5. (a) *J–V* curves, (b) EQE curves and (c) UV–Vis spectra of devices featuring P3HT:$PC_{61}BM$ layers prepared with thermal evaporation of 5.3-nm Au NDs and incorporating 50-nm Au NPs.

near-field effect. Chemically and lithographically fabricated metal NPs and nanostructures have been used widely in PSCs; fluorophores in close proximity to the metal NPs can result in excitation enhancement (increased light absorption), emission enhancement (increased radiative decay), or quenching (increased nonradiative decay) [30].

3.4. Steady state and dynamic photoluminescence results

To further estimate the influence of the LSPRs on the exciton generation, we performed the steady state and dynamic photoluminescence (PL) measurements and the corresponding results are shown in Fig. 6. Because P3HT predominately contributes to the light absorption and exciton generation in the P3HT:$PC_{61}BM$ active layer, we spin-coated the P3HT and P3HT:$PC_{61}BM$ films on PEDOT:PSS layer with thermally evaporated 5.3-nm Au NDs and incorporating 50-nm Au NPs.

Fig. 6a and b displays steady state PL spectra obtained using 470 and 550 nm excitation wavelengths; 550 nm excitation wavelength corresponds to the resonance peak of the LSPRs induced by Au NDs, 576 nm, and by Au NPs, 568 nm quite well. The P3HT films on PEDOT:PSS layer, however, has an absorption peak of 510 nm, and we would like to investigate the exciton life time from P3HT films, therefore, we chose 470 nm excitation wavelength for the time-resolved PL study. The PL intensity of these films was enhanced in both P3HT films and P3HT:$PC_{61}BM$ films that incorporate Au NDs and Au NPs when they were excited with 470 and 550 nm light, suggesting the increase of light absorption and exciton generation in P3HT upon the excitation of LSPRs. As a result of the resonance frequency of the Au NDs and Au NPs was close to the absorption band of P3HT, the PL intensity enhancement of P3HT can be attributed to the fact that excitation of the LSPRs increased the degree of light absorption and, thereby, enhanced the light excitation rate. Fig. 7 presents the PL

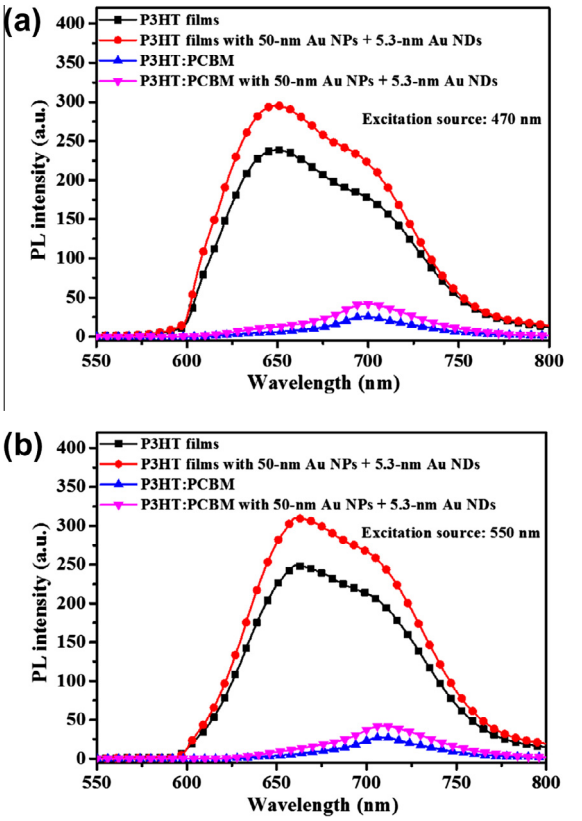

Fig. 6. Steady-state fluorescence spectra of P3HT and P3HT:$PC_{61}BM$ films incorporating thermally evaporated 5.3-nm Au NDs and embedded 50-nm Au NPs in the PEDOT:PSS layer using excitation wavelengths of (a) 470 and (b) 550 nm.

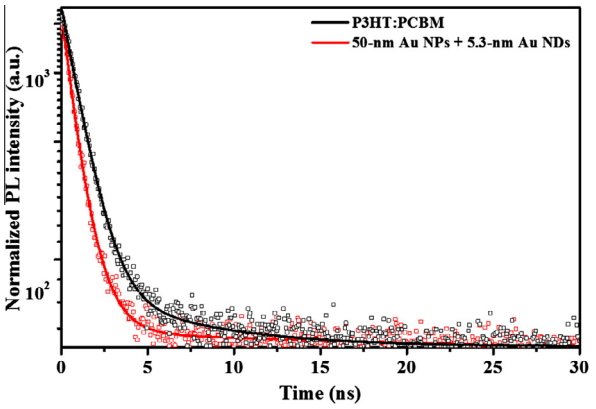

Fig. 7. Time-resolved PL spectra (detected at the wavelength of 650 nm via a 470 nm laser) of P3HT:$PC_{61}BM$ films presenting thermally evaporated 5.3-nm Au NDs and incorporating 50-nm Au NPs in the PEDOT:PSS layer.

intensity decay profiles, detected at the wavelength of 650 nm via a 470 nm laser of P3HT:$PC_{61}BM$ films with thermally evaporated 5.3-nm Au NDs on the top of P3HT films and incorporating 50-nm Au NPs in the PEDOT:PSS layer (plasmonic sample) and P3HT:$PC_{61}BM$ films (reference sample), the wavelength 650 nm was selected intentionally due to the greatest PL intensity in Fig. 6a.

We then performed a time-resolved photoluminescence (PL) study in which we determined the intensity of the PL, $I(t)$, using the following multi-exponential function [52]:

$$I(t) = \sum_{i=1}^{n} A_i e^{-\frac{T}{\tau_i}} \quad (1)$$

where A_i is the amplitude of the ith decay, n is the number of decays involved, and τ_i is the ith exponential constant. Fig. 7 presents the evolution of the intensity of the PL for various P3HT:$PC_{61}BM$ films; small changes in the exciton lifetimes ($\tau_{exciton}$) were evident for the samples prepared with and without dual plasmonic structures, implying the absence of strong coupling between the plasmonic field and the excitonic state. We analyzed the evolution of the PL intensity, $I(t)$, using Eq. (1) with two values for the lifetimes, τ_1 and τ_2, and corresponding amplitudes, A_1 and A_2. We then determined the average exciton lifetime ($\tau_{exciton}$) using the following equation:

$$\tau_{exciton} = \frac{A_1\tau_1^2 + A_2\tau_2^2}{A_1\tau_1 + A_2\tau_2} \quad (2)$$

For the reference sample, the values of the two fitted exponential constants τ_1 and τ_2 were 26.37 and 1.00 ns, respectively; they provided a corresponding exciton lifetime, $\tau_{exciton}$, of 11.20 ns. For the sample with dual plasmonic structure, the two exponential constants were 5.89, and 0.94 ns, respectively, providing $\tau_{exciton}$ of 1.69 ns. It suggests that the excitons were dissociated much faster at the presence of both Au NDs and Au NPs. This finding is consistent with previous reports of the plasmonic field strongly influencing photo induced charge separation or recombination processes through plasmon–exciton coupling [24,53,54].

4. Conclusion

Au NPs and Au NDs interact strongly with light through excitation of their localized surface plasmons; Au NPs incorporating into the PEDOT:PSS layer induced local field enhancement, not only leading to increased light absorption but also benefiting the photo induced charge separation processes, and Au NDs enhanced the parasitic absorption of light and an elevated degree of exciton dissociation. Accordingly, we have used both Au NPs and Au NDs to tune the resonance wavelength in PSC devices. We observed that the PCE of a dual LSPR device incorporating 5.3-nm Au NDs and 50-nm Au NPs blended in the PEDOT:PSS layer increased to 4.8% from a value of 4.0% for the corresponding P3HT:$PC_{61}BM$ cell lacking any Au particles. In the device incorporating 5.3-nm Au NDs, absorption dominated over the scattering of light; accordingly, PSCs fabricated with 5.3-nm Au NDs embedded between the absorber layer and the cathode exhibited the greatest enhancement in EQE among the tested Au ND systems. The Au NDs functioned as an effective medium layer that resulted in greater absorption of light by the P3HT:$PC_{61}BM$ film, resulting in enhanced exciton generation; when these excitons reached the P3HT-to-$PC_{61}BM$ interface, the degree of charge carrier dissociation also increased. Therefore, this specific type of Au NDs is suitable for the plasmonic enhancement of PSCs. We believe that such an approach, employing two types of localized surface plasmons, has the potential to result in PSC devices exhibiting even higher efficiencies.

Acknowledgements

We thank the National Science Council for financial support (NSC101-3113P-009-005) and Yin-Kai Lin for doing PL measurement.

Appendix A. Supplementary material

Supplementary data associated with this article can be found, in the online version, at http://dx.doi.org/10.1016/j.orgel.2013.06.012.

References

[1] J.Y. Kim, K. Lee, N.E. Coates, D. Moses, T.Q. Nguyen, M. Dante, A.J. Heeger, Efficient tandem polymer solar cells fabricated by all-solution processing, Science 317 (2007) 222–225.
[2] L.M. Chen, Z.R. Hong, G. Li, Y. Yang, Recent progress in polymer solar cells: manipulation of polymer: fullerene morphology and the formation of efficient inverted polymer solar cells, Adv. Mater. 21 (2009) 1434–1449.
[3] Y.W. Su, S.C. Lan, K.H. Wei, Organic photovoltaics, Mater. Today 15 (2012) 554–562.
[4] M.S. Su, C.Y. Kuo, M.C. Yuan, U.S. Jeng, C.J. Su, K.H. Wei, Improving device efficiency of polymer/fullerene bulk heterojunction solar cells through enhanced crystallinity and reduced grain boundaries induced by solvent additives, Adv. Mater. 23 (2011) 3315–3319.
[5] M.Y. Chiu, U.S. Jeng, M.S. Su, K.H. Wei, Morphologies of self-organizing regioregular conjugated polymer/fullerene aggregates in thin film solar cells, Macromolecules 43 (2010) 428–432.
[6] C.M. Liu, M.S. Su, J.M. Jiang, Y.W. Su, C.J. Su, C.Y. Chen, C.S. Tsao, K.H. Wei, Distribution of Crystalline Polymer and Fullerene Clusters in Both Horizontal and Vertical Directions of High-Efficiency Bulk

Heterojunction Solar Cells, ACS Appl. Mater. Interfaces 5 (2013) 5413–5422.
[7] G. Li, V. Shrotriya, J.S. Huang, Y. Yao, T. Moriarty, K. Emery, Y. Yang, High-efficiency solution processable polymer photovoltaic cells by self-organization of polymer blends, Nat. Mater. 4 (2005) 864–868.
[8] J.Y. Kim, S.H. Kim, H.H. Lee, K. Lee, W.L. Ma, X. Gong, A.J. Heeger, New architecture for high-efficiency polymer photovoltaic cells using solution-based titanium oxide as an optical spacer, Adv. Mater. 18 (2006) 572–576.
[9] M.C. Scharber, D. Wuhlbacher, M. Koppe, P. Denk, C. Waldauf, A.J. Heeger, C.L. Brabec, Design rules for donors in bulk-heterojunction solar cells – Towards 10% energy-conversion efficiency, Adv. Mater. 18 (2006) 789–794.
[10] M.D. Irwin, B. Buchholz, A.W. Hains, R.P.H. Chang, T.J. Marks, P-Type semiconducting nickel oxide as an efficiency-enhancing anode interfacial layer in polymer bulk-heterojunction solar cells, PNAS 105 (2008) 2783–2787.
[11] A. Kumar, G. Li, Z.R. Hong, Y. Yang, High efficiency polymer solar cells with vertically modulated nanoscale morphology, Nanotechnology 20 (2009) 165202.
[12] A.V. Zayats, I.I. Smolyaninov, A.A. Maradudin, Nano-optics of surface plasmon polaritons, Phys. Rep. 408 (2005) 131–314.
[13] K.L. Kelly, E. Coronado, L.L. Zhao, G.C. Schatz, The optical properties of metal nanoparticles: the influence of size, shape, and dielectric environment, J. Phys. Chem. B 107 (2003) 668–677.
[14] S. Link, M.A. El-Sayed, Size and temperature dependence of the plasmon absorption of colloidal gold nanoparticles, J. Phys. Chem. B 103 (1999) 4212–4217.
[15] W.L. Barnes, A. Dereux, T.W. Ebbesen, Surface plasmon subwavelength optics, Nature 424 (2003) 824–830.
[16] H. Raether, Springer Tr. Mod. Phys. 111 (1988) 1–133.
[17] J.P. Kottmann, O.J.F. Martin, D.R. Smith, S. Schultz, Plasmon resonances of silver nanowires with a nonregular cross section, Phys. Rev. B 64 (2001) 235402.
[18] K.R. Catchpole, A. Polman, Plasmonic solar cells, Opt. Express 16 (2008) 21793–21800.
[19] T.R. Jensen, M.D. Malinsky, C.L. Haynes, R.P. Van Duyne, Nanosphere lithography: tunable localized surface plasmon resonance spectra of silver nanoparticles, J. Phys. Chem. B 104 (2000) 10549–10556.
[20] S. Underwood, P. Mulvaney, Effect of the solution refractive-index on the color of gold colloids, Langmuir 10 (1994) 3427–3430.
[21] P. Mulvaney, Surface plasmon spectroscopy of nanosized metal particles, Langmuir 12 (1996) 788–800.
[22] S.A. Maier, H.A. Atwater, Plasmonics: localization and guiding of electromagnetic energy in metal/dielectric structures, J. Appl. Phys. 98 (2005) 011101.
[23] J.J. Mock, M. Barbic, D.R. Smith, D.A. Schultz, S. Schultz, Shape effects in plasmon resonance of individual colloidal silver nanoparticles, J. Chem. Phys. 116 (2002) 6755–6759.
[24] J.L. Wu, F.C. Chen, Y.S. Hsiao, F.C. Chien, P.L. Chen, C.H. Kuo, M.H. Huang, C.S. Hsu, Surface plasmonic effects of metallic nanoparticles on the performance of polymer bulk heterojunction solar cells, ACS Nano 5 (2011) 959–967.
[25] J. Yang, J.B. You, C.C. Chen, W.C. Hsu, H.R. Tan, X.W. Zhang, Z.R. Hong, Y. Yang, Plasmonic polymer tandem solar cell, ACS Nano 5 (2011) 6210–6217.
[26] A.J. Morfa, K.L. Rowlen, T.H. Reilly, M.J. Romero, J. van de Lagemaat, Plasmon-enhanced solar energy conversion in organic bulk heterojunction photovoltaics, Appl. Phys. Lett. 92 (2008) 013504.
[27] D.D.S. Fung, L.F. Qiao, W.C.H. Choy, C.D. Wang, W.E.I. Sha, F.X. Xie, S.L. He, Optical and electrical properties of efficiency enhanced polymer solar cells with Au nanoparticles in a PEDOT-PSS layer, J. Mater. Chem. 21 (2011) 16349–16356.
[28] C.H. Kim, S.H. Cha, S.C. Kim, M. Song, J. Lee, W.S. Shin, S.J. Moon, J.H. Bahng, N.A. Kotov, S.H. Jin, Silver nanowire embedded in P3HT: PCBM for high-efficiency hybrid photovoltaic device applications, ACS Nano 5 (2011) 3319–3325.
[29] J. Kim, G. Dantelle, A. Revaux, M. Berard, A. Huignard, T. Gacoin, J.P. Boilot, Plasmon-induced modification of fluorescent thin film emission nearby gold nanoparticle monolayers, Langmuir 26 (2010) 8842–8849.
[30] O. Stranik, R. Nooney, C. McDonagh, B.D. MacCraith, Optimization of nanoparticle size for plasmonic enhancement of fluorescence, Plasmonics 2 (2007) 15–22.
[31] F.C. Chen, J.L. Wu, C.L. Lee, Y. Hong, C.H. Kuo, M.H. Huang, Plasmonic-enhanced polymer photovoltaic devices incorporating solution-processable metal nanoparticles, Appl. Phys. Lett. 95 (2009) 013305.
[32] L. Lu, Z. Luo, T. Xu, L. Yu, Cooperative plasmonic effect of Ag and Au nanoparticles on enhancing performance of polymer solar cells, Nano Lett. 13 (2012) 59–64.
[33] J.H. Lee, J.H. Park, J.S. Kim, D.Y. Lee, K. Cho, High efficiency polymer solar cells with wet deposited plasmonic gold nanodots, Org. Electron. 10 (2009) 416–420.
[34] A.Y. Mahmouda, J. Zhang, D. Ma, R. Izquierdo, V.V. Truong, Optically-enhanced performance of polymer solar cells with low concentration of gold nanorods in the anodic buffer layer, Org. Electron. 13 (2012) 3102–3107.
[35] D.H. Wang, D.Y. Kim, K.W. Choi, J.H. Seo, S.H. Im, J.H. Park, O.O. Park, A.J. Heeger, Enhancement of donor-acceptor polymer bulk heterojunction solar cell power conversion efficiencies by addition of au nanoparticles, Angew. Chem. Int. Ed. 50 (2011) 5519–5523.
[36] D.H. Wang, K.H. Park, J.H. Seo, J. Seifter, J.H. Jeon, J.K. Kim, J.H. Park, O.O. Park, A.J. Heeger, Enhanced power conversion efficiency in PCDTBT/PC70BM bulk heterojunction photovoltaic devices with embedded silver nanoparticle clusters, Adv. Energy Mater. 1 (2011) 766–770.
[37] B. Paci, G.D. Spyropoulos, A. Generosi, D. Bailo, V.R. Albertini, E. Stratakis, E. Kymakis, Enhanced structural stability and performance durability of bulk heterojunction photovoltaic devices incorporating metallic nanoparticles, Adv. Funct. Mater. 21 (2011) 3573–3582.
[38] X.H. Li, W.C.H. Choy, L.J. Huo, F.X. Xie, W.E.I. Sha, B.F. Ding, X. Guo, Y.F. Li, J.H. Hou, J.B. You, Y. Yang, Dual plasmonic nanostructures for high performance inverted organic solar cells, Adv. Mater. 24 (2012) 3046–3052.
[39] A.P. Kulkarni, K.M. Noone, K. Munechika, S.R. Guyer, D.S. Ginger, Plasmon-enhanced charge carrier generation in organic photovoltaic films using silver nanoprisms, Nano Lett. 10 (2010) 1501–1505.
[40] H.A. Atwater, A. Polman, Plasmonics for improved photovoltaic devices, Nat. Mater. 9 (2010) 205–213.
[41] N. Kalfagiannis, P.G. Karagiannidis, C. Pitsalidis, N.T. Panagiotopoulos, C. Gravalidis, S. Kassavetis, P. Patsalas, S. Logothetidis, Plasmonic silver nanoparticles for improved organic solar cells, Sol. Energy Mat. Sol. Cells 104 (2012) 165–174.
[42] S. Eustis, M.A. El-Sayed, Why gold nanoparticles are more precious than pretty gold: noble metal surface plasmon resonance and its enhancement of the radiative and nonradiative properties of nanocrystals of different shapes, Chem. Soc. Rev. 35 (2006) 209–217.
[43] A.N. Shipway, E. Katz, I. Willner, Nanoparticle arrays on surfaces for electronic, optical, and sensor applications, Chemphyschem 1 (2000) 18–52.
[44] E. Hutter, J.H. Fendler, Exploitation of localized surface plasmon resonance, Adv. Mater. 16 (2004) 1685–1706.
[45] T. Okamoto, I. Yamaguchi, T. Kobayashi, Local plasmon sensor with gold colloid monolayers deposited upon glass substrates, Opt. Lett. 25 (2000) 372–374.
[46] A. Doron, E. Katz, I. Willner, Organization of au colloids as monolayer films onto ITO glass surfaces – application of the metal colloid films as base interfaces to construct redox-active monolayers, Langmuir 11 (1995) 1313–1317.
[47] K.C. Grabar, P.C. Smith, M.D. Musick, J.A. Davis, D.G. Walter, M.A. Jackson, A.P. Guthrie, M.J. Natan, Kinetic control of interparticle spacing in Au colloid-based surfaces: rational nanometer-scale architecture, J. Am. Chem. Soc. 118 (1996) 1148–1153.
[48] S.W. Kennerly, J.W. Little, R.J. Warmack, T.L. Ferrell, Optical-properties of heated Ag films, Phys. Rev. B 29 (1984) 2926–2929.
[49] R. Chauvaux, A. Meessen, Multipole oscillations in small hemispherical particles, Thin Solid Films 62 (1979) 125–131.
[50] R.J. Warmack, S.L. Humphrey, Observation of 2 surface-plasmon modes on gold particles, Phys. Rev. B 34 (1986) 2246–2252.
[51] C.C. Chang, H.L. Wu, C.H. Kuo, M.H. Huang, Hydrothermal synthesis of monodispersed octahedral gold nanocrystals with five different size ranges and their self-assembled structures, Chem. Mater. 20 (2008) 7570–7574.
[52] M. Jones, J. Nedeljkovic, R.J. Ellingson, A.J. Nozik, G. Rumbles, Photoenhancement of luminescence in colloidal CdSe quantum dot solutions, J. Phys. Chem. B 107 (2003) 11346–11352.
[53] H. Ohkita, S. Cook, Y. Astuti, W. Duffy, S. Tierney, W. Zhang, M. Heeney, I. McCulloch, J. Nelson, D.D.C. Bradley, J.R. Durrant, Charge carrier formation in polythiophene/fullerene blend films studied by transient absorption spectroscopy, J. Am. Chem. Soc. 130 (2008) 3030–3042.
[54] N.T. Fofang, T.H. Park, O. Neumann, N.A. Mirin, P. Nordlander, N.J. Halas, Plexcitonic nanoparticles: plasmon-exciton coupling in nanoshell-J-aggregate complexes, Nano Lett. 8 (2008) 3481–3487.